Palaeogeography, Palaeoclimatology, Palaeoecology 702 (2026) 114210

Contents lists available at ScienceDirect

Palaeogeography, Palaeoclimatology, Palaeoecology

journal homepage: www.elsevier.com/locate/palaeo

A quality-screened Holocene relative sea-level database for the northern South China Sea and evidence for a mid-Holocene highstand☆

Yuanfu Yue[a,**], Bo Zhang[a], Lichao Tang[a,b,*], Yiheng Zhao[a], Jie Wang[b], Ruizhe Yang[b]

[a] *Guangxi Laboratory on the Study of Coral Reefs in the South China Sea, Coral Reef Research Center of China, School of Marine Sciences, Guangxi University, Nanning 530004, China*

[b] *Ministry of Education Key Laboratory for Coast and Island Development, School of Geography and Ocean Science, Nanjing University, Nanjing 210093, China*

ARTICLE INFO

Editor: M Elliot

Keywords:
South China Sea
Holocene
Relative sea level
Sea-level index points
Mid-Holocene highstand
Coral microatolls
Beachrock

ABSTRACT

Holocene relative sea-level (RSL) evolution across the northern South China Sea (SCS) remains highly debated, especially regarding the timing, magnitude and duration of the mid-Holocene highstand. Existing disagreements are likely influenced by differences in data quality and the interpretation of sea-level proxies, as previous compilations have rarely applied unified quality screening and comprehensive uncertainty quantification to sea-level index points (SLIPs) and marine- and terrestrial-limiting data. In this work, we systematically compiled 374 published records (including SLIPs and limiting data), standardized their depositional metadata and uncertainty parameters, and retained 146 records for the primary reconstruction after multi-criteria quality filtering. We then reconstructed Holocene RSL evolution using an errors-in-variables integrated Gaussian process (EIV-IGP) Bayesian model, and compared modeled outputs with far-field glacial isostatic adjustment (GIA) predictions from two ICE-6G_C-based model configurations. The reconstruction showed a rapid RSL rise during the early Holocene. RSL then remained above present from 7.0 to 3.4 cal ka BP, with the best-constrained estimates indicating a peak within the range of 1.4–2.6 m. In situ *Porites* microatolls and intact stratigraphic beachrocks delivered the most robust highstand constraints, while shell and organic muddy deposits only provided low-precision, broad limiting bounds. Mismatches between reconstructed RSL and GIA curves were interpreted as composite residuals that may reflect GIA model uncertainty, regional vertical land motion, sediment compaction, and residual proxy uncertainties. This study provides a standardized and reproducible SLIP database for the northern SCS with explicit uncertainty estimates. The results indicate that differences in proxy reliability contribute substantially to the long-standing regional disagreement, while the quality-screened reconstruction supports a coherent mid-Holocene highstand along western Pacific far-field coasts.

1. Introduction

Relative sea-level (RSL) change during the Holocene provides a critical geological boundary condition for reconstructing coastal evolution, testing coupled ice-sheet-Earth-ocean system models, and evaluating the natural range of sea-level variability prior to the instrumental era. In far-field regions, RSL histories reflect the combined effects of global ice-volume change and gravitationally self-consistent ocean loading, the resulting glacial- and hydro-isostatic responses, vertical land motion, and coastal local processes such as sediment compaction (Bradley et al., 2016; Clark et al., 1978; Lambeck et al., 2014; Mitrovica and Milne, 2002). Consequently, high-quality Holocene RSL databases are most useful when they explicitly distinguish sea-level index points (SLIPs) from marine- and terrestrial-limiting data, quantify both age and elevation uncertainties, and document the indicative meaning of each proxy (Khan et al., 2015; Shennan and Horton, 2002). Such standardized RSL archives provide an essential geological baseline for assessing modern sea-level change in the context of natural Holocene variability (Lin et al., 2025). As a low-latitude far-field basin in the western Pacific, the northern South China Sea (SCS) is particularly valuable because its

☆ This article is part of a Special issue entitled: ‘Neogene-Quaternary’ published in Palaeogeography, Palaeoclimatology, Palaeoecology.

* Corresponding author at: Guangxi Laboratory on the Study of Coral Reefs in the South China Sea, Coral Reef Research Center of China, School of Marine Sciences, Guangxi University, Nanning 530004, China.

** Corresponding author.

E-mail addresses: yuanfu.yue@gxu.edu.cn (Y. Yue), tanglichao2020@163.com (L. Tang).

https://doi.org/10.1016/j.palaeo.2026.114210
Received 10 June 2026; Received in revised form 15 August 2026; Accepted 6 September 2026
Available online 8 September 2026
0031-0182/© 2026 Elsevier B.V. All rights are reserved, including those for text and data mining, AI training, and similar technologies.

geological records provide an important complement to the limited tropical constraints available for evaluating glacial isostatic adjustment (GIA) models and reconstructing past ice-volume histories.

Against this global methodological framework, the northern SCS (Fig. 1a, b) provides a suitable setting for applying and evaluating standardized SLIP reconstruction workflows, owing to its diverse coastal geomorphic and sedimentary archives. It occupies a low-latitude, far-field setting on the western Pacific margin and includes a geomorphically diverse coastline comprising estuaries, deltas, rocky shorelines, coral reef coasts, and sheltered embayments (Fig. 1c). This diversity has generated a wide spectrum of potential sea-level indicators, including in situ coral reefs, *Porites* microatolls, beachrock, shell accumulations, tidal-flat deposits, mangrove-related organic sediments, and lagoonal or brackish-water sequences (Yue et al., 2024, 2025; Yue and Tang, 2023; Tang and Yue, 2023; Xiong et al., 2018; Zong, 2004). Meanwhile, regional environmental and depositional processes, including East Asian monsoon variability, riverine sediment supply, and shelf circulation, can influence the depositional and ecological settings in which sea-level indicators form and are preserved (An, 2000; Yin et al., 2021).

Despite long-standing interest in the region, no consensus has been reached on the shape of the northern SCS Holocene RSL curve. Coral reef

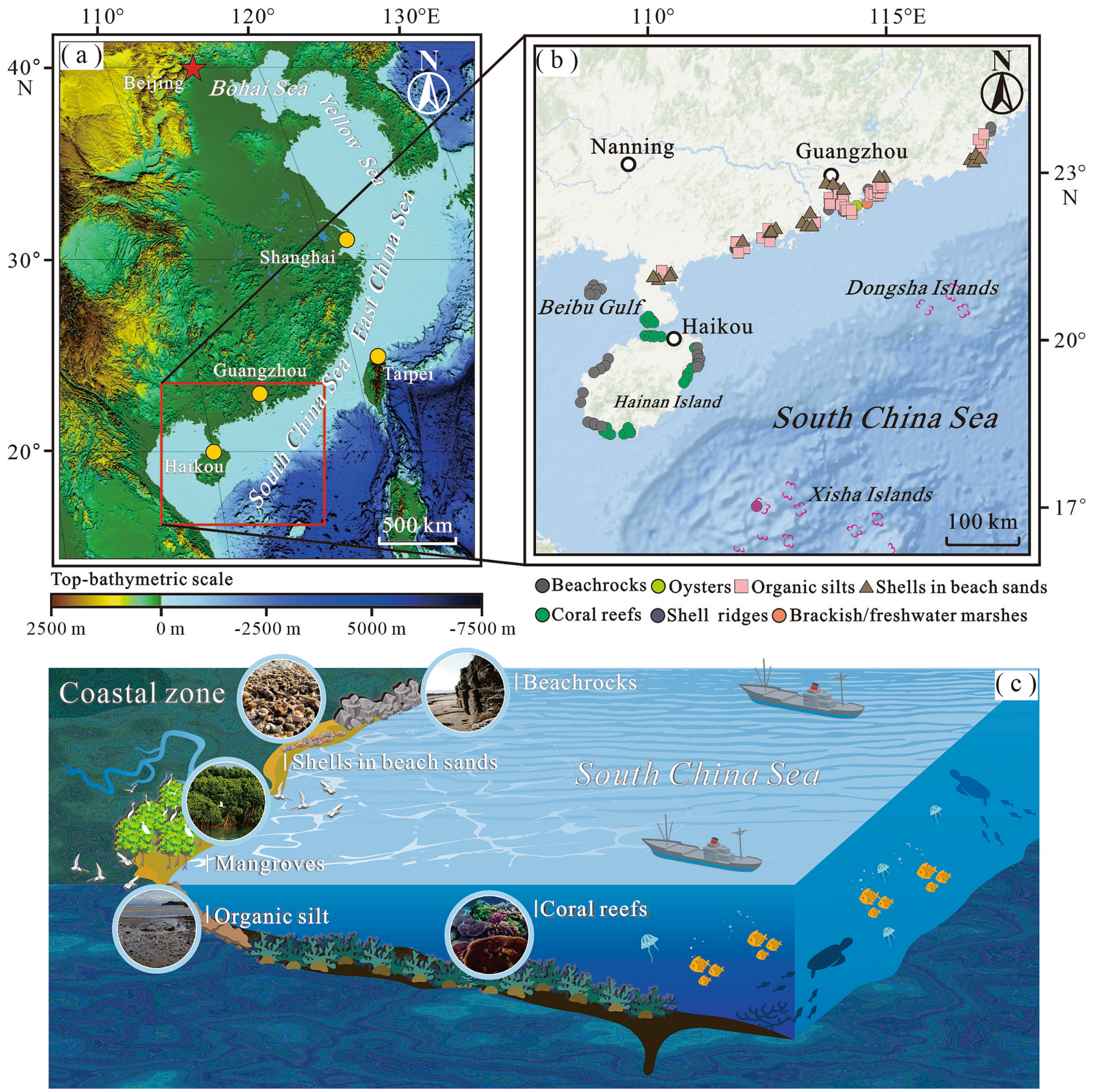

Fig. 1. Study area, spatial distribution and depositional context of quality-screened Holocene SLIPs and limiting data in the northern SCS. (a) Geographic location of the study area in the western Pacific; (b) spatial distribution of seven proxy classes across the Beibu Gulf coast, Hainan Island, Leizhou Peninsula, Pearl River Delta and eastern Guangdong coast; (c) schematic cross-section showing the typical depositional water depths and tidal positions of coral reefs, beachrock, shell deposits, mangroves and organic silts.

and other intertidal indicators with relatively narrow indicative ranges have been used to argue for a mid-Holocene highstand, with some coral-based reconstructions indicating RSL elevations of up to approximately 2 m above present (Yue et al., 2024; Yu et al., 2009). However, substantially different RSL histories have also been reconstructed depending on how the indicative meaning of coral indicators is defined and calibrated (Yue et al., 2024, 2025). Other regional syntheses based on geological indicators have yielded more muted mid-Holocene RSL signals, including no clear higher-than-present highstand in some reconstructions (Xiong et al., 2018), whereas broader syntheses emphasize substantial spatial variability in the timing and magnitude of Holocene highstands along the southeastern Chinese coast (Zong, 2004). More recent regional-scale modelling further indicates that late-Holocene RSL variability can reflect a combination of global mean sea-level stabilization and regional-to-local processes, including tectonic and sedimentary effects (Lin et al., 2025). These discrepancies may therefore arise from both genuine geological heterogeneity among coastal environments and differences in proxy selection, data screening, and analytical procedures. Sea-level proxies differ substantially in their indicative ranges, susceptibility to sediment reworking and compaction, and chronological precision. Consequently, regional reconstructions that combine published observations without explicitly accounting for these differences risk mixing robust SLIPs with limiting data and sedimentary records affected by post-depositional processes.

Beyond the disputed mid-Holocene amplitude, the late-Holocene trajectory also remains controversial. Some reconstructions suggest relatively stable RSL after the mid-Holocene maximum (Lin et al., 2025), whereas others record a gradual, albeit fluctuating, decline toward the present sea level (Yue and Tang, 2023;Yan et al., 2021). This divergence is particularly pronounced in low-gradient coastal plains, where sediment compaction and local tectonic subsidence can alter the preserved elevations of sea-level indicators, while spatially variable accommodation space complicates their stratigraphic interpretation (Fu et al., 2020; Xiong et al., 2018; Törnqvist et al., 2004).

Even if regional RSL trends can be reliably reconstructed, a third critical question concerns the mechanisms driving the reconstructed RSL variations. Previous studies have attributed northern SCS variability to a combination of global ice-volume change and far-field GIA, while regional tectonic deformation and sedimentary processes may further modify the preserved RSL signal (Yue et al., 2025; Bradley et al., 2016; Contreras-Rosales et al., 2019; Tang et al., 2011). Regional hydroclimatic and oceanographic variability may additionally influence the depositional and ecological settings in which sea-level indicators are preserved (An, 2000; Yin et al., 2021; Contreras-Rosales et al., 2019). These processes are not mutually exclusive, and meter-scale RSL variations on millennial timescales during the Holocene are expected to be strongly influenced by global ice-volume change and GIA in low-latitude far-field settings. Regional monsoon and sea-surface temperature (SST) variability may additionally influence coastal hydrodynamics, sediment delivery, and proxy preservation, but their contributions to long-term RSL variability require explicit evaluation.

To address these methodological limitations and outstanding scientific questions, this study compiled and standardized 374 published Holocene sea-level records, including SLIPs and limiting data, from the northern SCS; applied explicit screening criteria for chronological, vertical and contextual reliability; and reconstructed a probabilistic continuous RSL history using the errors-in-variables integrated Gaussian process (EIV-IGP) model. The study evaluates which proxy classes meet the criteria for robust SLIPs with well-constrained indicative meaning and which should be retained only as limiting evidence. It then tests whether the quality-screened dataset supports a mid-Holocene RSL highstand above present sea level, whether this signal remains robust when compaction-prone lowland deposits are excluded, and how the reconstructed RSL trajectory compares with far-field GIA predictions to constrain the interpretation of model–data residuals.

2. Regional setting

Geomorphologically, the northern SCS hosts diverse coastal environments, from large deltaic plains (e.g., the Pearl River Delta) to rocky and reef-fringed coasts (e.g., Hainan Island and the Leizhou Peninsula). This geomorphic heterogeneity strongly influences the formation, preservation, and post-depositional modification of SLIPs. Coral-based indicators are concentrated mainly around Hainan Island and the Leizhou Peninsula (Yan et al., 2024; Yu and Chen, 2009; Yue et al., 2024, 2025), whereas tidal-flat sediments, shell-bearing deposits, and organic silts are more commonly preserved in low-gradient coastal plains and estuarine basins (Xiong et al., 2018; Zong, 2004). This spatial separation of proxy types forms the basis for our database compilation and quality classification (Fig. 1, Table S1).

The oceanographic and monsoon systems of the northern SCS modulate coastal sedimentation and reef growth, and thus affect the preservation of SLIPs. Seasonal monsoon forcing influences the hydrographic and sedimentary environment of the northern SCS, while terrigenous sediment inputs from riverine and local watersheds contribute to coastal deposition (An, 2000; He et al., 2024; You et al., 2024). On orbital to centennial timescales, long-term monsoon variability altered runoff and salinity conditions, which modified the depositional context of sedimentary proxies and the ecological window for coral growth (Zhang et al., 2023).

The northern SCS is not tectonically or sedimentologically uniform across subregions. Differential subsidence, fault-related deformation, sediment compaction, and anthropogenic disturbance can all alter the original elevation of sea-level proxies, particularly in the Pearl River Delta and other lowland coastal plains (Xiong et al., 2018; Fu et al., 2020). Such regional geological heterogeneity prevents one-to-one interpretation of GIA residuals. Differences between the modeled curves and field data may arise from several sources, including GIA model uncertainty, vertical land motion, sediment compaction, datum errors, and proxy-specific measurement uncertainty.

Despite these complexities, the region is well suited for Holocene RSL reconstruction because it hosts both high-precision biogenic proxies (in situ coral reefs and *Porites* microatolls, Yue et al., 2024, 2025) and abundant sedimentary indicators (Xiong et al., 2018). In situ corals have narrow indicative ranges and can be dated by U-series methods (Yue et al., 2024, 2025), whereas stratigraphically secure beachrock provides reliable intertidal shoreline constraints (Tang and Yue, 2023; Tang et al., 2011).

3. Materials and methods

3.1. Data compilation and database structure

We compiled 374 published Holocene sea-level records from the northern SCS into a standardized, traceable database (Table S1). Each record is assigned a unique ID and structured metadata fields. These include subregion, site coordinates, proxy class, dated material, depositional context, dating method, raw laboratory age, calibrated age (2σ uncertainty), measured elevation, vertical datum, indicative meaning, indicative range, total vertical uncertainty, data classification (SLIP / marine-limiting / terrestrial-limiting), and original reference.

The full master database (Table S1) includes all 374 compiled records, with exclusion reasons explicitly marked for records not used in the primary reconstruction. The screened subset of 146 SLIPs used for EIV-IGP modelling is provided separately in Table S2, linked to the master database via the unique record ID.

Original studies used inconsistent terminology and reporting standards, so all entries were harmonized before modelling. Records with missing or internally inconsistent coordinates, ambiguous vertical datum, unclear depositional context, unresolved sample integrity or insufficient information to define indicative meaning were retained in the master database for transparency but excluded from the primary

EIV-IGP likelihood.

The database is dominated by four proxy groups relevant to the primary reconstruction: coral reefs, beachrock, shells in coastal deposits, and organic silts from tidal or marginal-marine settings. A smaller number of shell ridges, oysters, and brackish/freshwater marsh indicators were also compiled, but most of these were treated as limiting data rather than as strong index points because their indicative ranges are broad or their depositional settings are difficult to constrain precisely.

3.2. Classification of SLIPs and indicative meaning

Following standard global mean sea level (GMSL) database protocols (Engelhart and Horton, 2012; Shennan and Horton, 2002; Vacchi et al., 2016), each record was classified as one of three categories based on its ability to constrain former RSL. A SLIP is a record with well-constrained age and a quantifiable vertical relationship to contemporaneous RSL, based on clear depositional or ecological evidence. A marine-limiting datum is a record demonstrating that former RSL was above the sampled elevation, but without a precise upper bound. A terrestrial-limiting datum is a record demonstrating that former RSL was below the sampled elevation, but without a precise lower bound. Classification was evaluated independently of eligibility for the primary reconstruction. A record classified as a SLIP may still be excluded from modelling if it fails chronological, elevational or contextual quality screening (Section 3.4).

Indicative meaning was assigned from site-specific depositional, ecological or geomorphic context. For coral indicators, particularly *Porites* microatolls and in situ massive *Porites* colonies, the relevant reference level is the upper growth limit relative to local tidal levels; the indicative range is therefore narrow only when the fossil growth surface is preserved, the colony is demonstrably in situ and the modern ecological analogue has been locally calibrated (Yue et al., 2024, 2025; Yu and Chen, 2009). Beachrock was treated as an intertidal indicator only where primary cementation fabric, stratigraphic position and geomorphic context support in situ formation; otherwise, it was treated as lower-confidence or limiting evidence.

Shells and shell-rich coastal deposits were treated more cautiously. Although they may indicate intertidal or shallow subtidal conditions, reworking, transport, and time averaging can substantially widen their indicative range. Likewise, organic silts and peaty or brackish deposits can mark marginal-marine environments, but they are highly vulnerable to compaction and often lack a sufficiently narrow vertical relation to sea level to justify treatment as precise index points. Accordingly, shells and organic silts were retained primarily where stratigraphic context was unusually good and uncertainty could be explicitly evaluated.

3.3. Chronological standardization and age calibration

The compiled dataset includes conventional radiocarbon ages, AMS ^{14}C ages and U-Th coral ages. Radiocarbon ages were recalibrated using CALIB 8.2 with IntCal20 for terrestrial organic material and Marine20 calibration curve for marine shells, coral fragments and beachrock carbonates, supplemented by regional marine reservoir corrections (ΔR) reported by Yu et al., 2010. All calibrated ages are referenced to 1950 CE. Individual calibrated ages are reported in cal yr BP, while millennial-scale trends are described in cal ka BP, both at 2σ uncertainty.

U-Th ages from coral material were retained only where the original study reported analytical quality and diagenetic screening, or where such assessment was possible from the provided metadata. For coral-based SLIPs, U-Th dating offers the strongest chronological control in this compilation, but reliability still depends on closed-system behavior, preservation of the dated growth surface, low detrital contamination and clear evidence that the dated coral is in growth position (Stirling and Andersen, 2009).

Chronological screening balanced temporal resolution against data retention. Records with 2σ age uncertainties greater than 180 yr were excluded from the primary reconstruction unless they were used only as limiting or contextual evidence.

3.4. Elevation standardization, uncertainty propagation, and quality screening

RSL elevation for each SLIP was calculated as: RSL = measured elevation − indicative meaning midpoint, where positive values indicate former RSL above the modern datum. All records were flagged for datum quality; those with undocumented or unresolvable vertical datums were excluded from the primary reconstruction.

Following standard SLIP practice (Shennan and Horton, 2002), total vertical uncertainty was propagated from five independent components—instrumental measurement error, datum conversion error, indicative range uncertainty, sample position uncertainty, and contextual depositional uncertainty—using the root-sum-of-squares method.

Where original studies reported measured uncertainties, these values were adopted directly. For records without reported measurement errors, we assigned conservative proxy-specific empirical values based on regional published estimates (Zong, 2004; Xiong et al., 2018), all of which were flagged in the database. Elevations of records from our previous field campaigns were measured via real-time kinematic (RTK) GNSS tied to the 1985 National Height Datum, with a nominal instrumental uncertainty of 0.05 m (Yue et al., 2024, 2025).

The vertical-uncertainty components were quantified using information from the original publications and proxy-specific interpretations. Elevation-measurement uncertainties were adopted directly from the original studies wherever they were reported. For records obtained from other published studies, the reported survey precision or elevation uncertainty was used where available.

The indicative meaning and indicative range of each proxy were determined from the depositional or ecological interpretation given in the original publication, supplemented by proxy-specific indicative frameworks (Shennan and Horton, 2002; Vacchi et al., 2016; Zong, 2004). Thus, the indicative uncertainty was not assigned solely from a uniform value for each proxy class; rather, it was evaluated according to the reported formation environment and the relationship of the indicator to local tidal levels. Where the original study provided sufficient information, the reference water level and indicative range were recalculated or standardized to the common vertical reference used in this study.

All records were subjected to a multi-step quality-screening procedure. Records were excluded from the primary reconstruction if they met any of the following criteria: insufficient contextual information to define indicative meaning; evidence of reworking or redeposition; 2σ age uncertainty exceeding 180 yr; vertical uncertainty exceeding 0.8 m; unresolvable datum or coordinate problems; or inconsistency with their inferred depositional setting. Retained records were assigned confidence classes, with high confidence for in situ coral indicators and well-preserved in situ beachrock, intermediate confidence for stratigraphically secure shell-bearing or tidal-flat records, and low confidence for broad-range or compaction-prone organic and muddy deposits.

The selection of records retained for the final reconstruction followed established protocols for geological sea-level databases. These protocols include distinguishing SLIPs from upper- and lower-limiting data, explicitly defining the indicative meaning of each proxy, evaluating sample integrity and depositional context, standardizing chronological information, harmonizing elevation datums, and propagating age and vertical uncertainties (Engelhart and Horton, 2012; Hijma et al., 2015, 2025).

A record qualifies as a valid SLIP only if its age and palaeo-water-level offset are fully constrained by depositional or ecological evidence. Any sample lacking clear tidal reference bounds, showing reworked sedimentary fabrics, or whose dated material is stratigraphically disconnected from the SLIP is excluded from core modelling and reclassified as limiting data.

Application of these criteria to the 374-record master database resulted in 146 records being retained for the primary reconstruction and 228 records being excluded from the primary reconstruction. Because some records failed more than one screening criterion, each excluded record was assigned a single primary exclusion category according to the first criterion triggered in the screening workflow (Table S1). The exclusion categories and their corresponding codes are summarized in Table S1.

The largest group of excluded records (86 records) lacked sufficient stratigraphic documentation to establish credible tidal-indicative ranges (E1). Other exclusion categories included reworked coral or shell material (2 records; E2), excessive chronological uncertainty (53 records; E3), and large vertical uncertainty (3 records; E4).

No records were excluded because of unresolved geographic coordinates or vertical datums (E5). Three records were excluded because their proxy interpretations were inconsistent with the depositional facies reported in the original publications (E6).

Beyond these exclusion categories, 6 duplicate records were removed from the master database (D0). A further 75 records were retained in the master database as marine- or terrestrial-limiting data but were not included in the primary EIV-IGP reconstruction (L1). Thus, the 146 retained records represent 39.0% of the original compilation.

3.5. EIV-IGP reconstruction of Holocene RSL

Continuous Holocene RSL change was reconstructed using the errors-in-variables integrated Gaussian process (EIV-IGP) model developed by Cahill et al. (2015), which accounts for both age and elevation uncertainty in input data and avoids artefacts from deterministic curve-fitting. The model places a Gaussian process prior on the rate of RSL change, then integrates the rate process to derive the RSL trajectory. Bayesian inference is implemented via Markov Chain Monte Carlo (MCMC) sampling to produce posterior estimates of RSL and its uncertainty through time.

We applied the published model code to our screened 146 SLIPs, using a squared exponential covariance function for the rate process. MCMC sampling was run with 3 chains of 100,000 iterations each, with the first 50,000 iterations discarded as burn-in and a thinning rate of 10. Convergence was assessed using the Gelman-Rubin statistic ($\hat{R} < 1.1$ for all parameters). The model was implemented in R and JAGS. Full model parameters and convergence diagnostics are provided in Supplementary Methods Section 2.2.

3.6. Comparison with glacial isostatic adjustment predictions

To evaluate the reconstructed RSL history in a far-field context, we compared our geological reconstruction with GIA predictions based on two Earth-model configurations. The first combines the ICE-6G_C ice history with the VM5a Earth model (Peltier et al., 2015), whereas the second couples the same ICE-6G_C ice history with the three-dimensional, laterally heterogeneous Earth model HetML140 (Li and Wu, 2019). The model configurations and regional application were informed by previous GIA studies of the Chinese coast (Xiong et al., 2018, 2020). GIA predictions were extracted for three representative subregions: Hainan Island, Leizhou Peninsula, and Pearl River Delta.

This comparison serves as a benchmark for expected far-field RSL behavior, not as a deterministic correction for local vertical land motion. Model-data residuals are interpreted as composite offsets integrating GIA structural uncertainty, tectonic vertical land motion, sediment compaction, datum error, and proxy uncertainty, rather than direct measures of tectonic subsidence.

4. Results

4.1. Composition of the compiled and screened database

The compiled master database comprises 374 Holocene sea-level records, ranging from 9.7 cal ka BP to the present, and encompasses multiple regions across the northern SCS (Fig. 2a, b). Proxy classes are distributed as follows (Fig. 2c): 120 coral reef records (32.09%), 99 beachrock records (26.47%), 87 tidal/mudflat deposits (23.26%), 56 shell-bearing coastal deposits (14.97%), 6 shell ridges (1.60%), 5 oyster records (1.34%), and 1 brackish-freshwater marsh record (0.27%).

After multi-criteria quality screening, 146 records (39.0% of the full database) were retained for the primary EIV-IGP reconstruction. The screened subset is dominated by high-confidence proxies: 87 coral-reef records (59.6%), 35 beachrock records (24.0%), 14 tidal or muddy coastal deposits (9.6%), and 10 shell-bearing coastal records (6.8%). Retention rates differ markedly across proxy classes, reflecting inherent differences in data quality and contextual documentation.

Chronologically, the retained dataset is much denser during the mid-Holocene than during the early Holocene. High-quality reef-based indicators are concentrated during 7–4 cal ka BP, whereas earlier intervals rely more heavily on broader and more scattered sedimentary records. This asymmetry is important: the timing and elevation of the mid-Holocene highstand are comparatively well constrained, but the precise shape of early Holocene RSL rise remains more uncertain.

4.2. Spatial and temporal distribution of the retained records

The spatial distribution of retained records is strongly structured by coastal geomorphology. Hainan Island and the Leizhou Peninsula contribute the majority of the high-confidence coral and beachrock records (Fig. 2b). The Pearl River Delta and adjacent Guangdong lowlands contribute a larger proportion of shell-bearing and organic or muddy sedimentary indicators. The Beibu Gulf contains fewer total records, many of which are beachrock or diatom/sediment-based constraints from the mid to late Holocene.

Temporally, only 12 retained records predate 8.0 cal ka BP, all from sedimentary and shell proxies with relatively large uncertainties. The number of records increases sharply after 7.0 cal ka BP, peaks between 6.5 and 4.0 cal ka BP (95 records, 65.1% of the screened subset), and declines gradually after 3.0 cal ka BP. This temporal clustering drives the narrower uncertainty envelope during the mid-Holocene highstand phase, and the wider uncertainty in the early and late Holocene (Section 4.4).

4.3. Proxy-specific patterns and relative reliability

Proxy classes differ significantly in both chronological and vertical precision (Kruskal–Wallis test, $p < 0.001$ for both) (Fig. 3). In situ coral records, especially *Porites* microatolls and massive *Porites* colonies with preserved upper growth surfaces, have the narrowest indicative ranges (median vertical uncertainty = 0.098 m) and highest dating precision (median 2σ age uncertainty <100 yr for U-series dated samples). The narrow indicative meaning of well-preserved in situ Porites growth surfaces has been demonstrated in previous regional studies (Yue et al., 2024, 2025). Beachrock records have intermediate precision (median vertical uncertainty = 0.350 m), while shell-bearing and organic silt deposits have significantly wider uncertainties (median vertical uncertainty = 0.500 m and 0.650 m, respectively) due to reworking potential and compaction effects.

Across the 7.6–5.0 cal ka BP window covering the peak highstand (Fig. 3), the highest RSL estimates (~2.6 m above present) all come from in situ coral records with well-constrained indicative meanings. Toward 5.0 cal ka BP, RSL estimates from all proxy classes show a gradual declining trend, consistent with the model-reconstructed trajectory.

Beachrock also provides relatively robust constraints, particularly

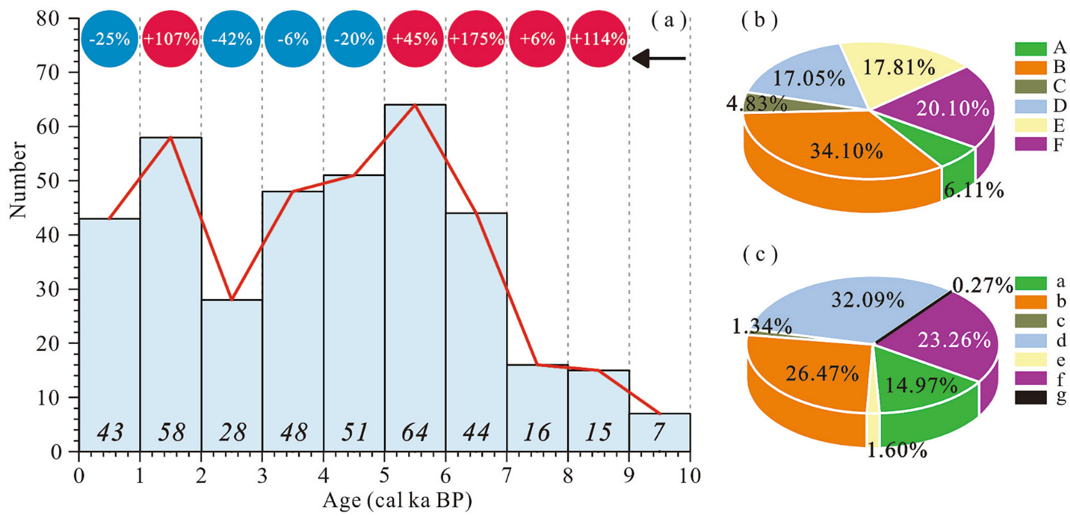

Fig. 2. Spatiotemporal distribution of Holocene SLIPs in the northern SCS. (a) Temporal distribution of the SLIPs. The percentages above the bars indicate the percentage change in the number of SLIPs assigned to each 1-kyr interval relative to the immediately preceding 1-kyr interval, calculated as $[(N_i - N_{i-1})/N_{i-1}] \times 100\%$. Positive values indicate increases, whereas negative values indicate decreases. (b) Spatial distribution of the SLIPs, with A–F denoting the Beibu Gulf, Hainan Island, the Leizhou Peninsula, East Guangdong, West Guangdong, and the Pearl River Delta, respectively. (c) Proportions of the different SLIP types.

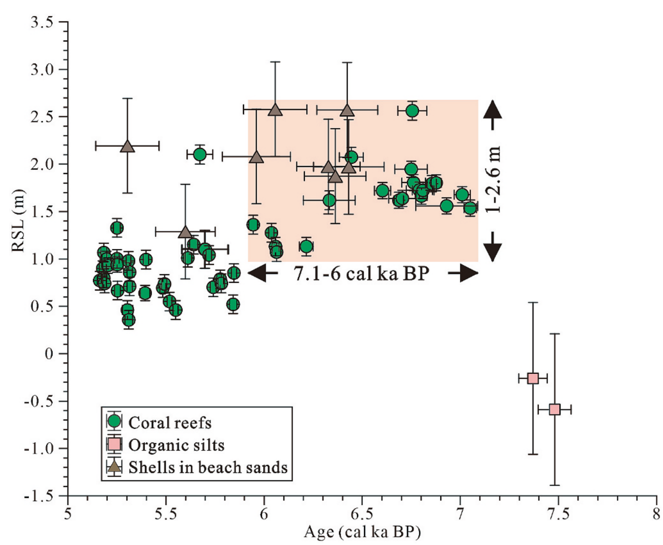

Fig. 3. Proxy-specific RSL estimates from 7.6 to 5.0 cal ka BP, covering the interval of the highest mid-Holocene sea level and the initial subsequent decline. Symbols and colors distinguish coral reefs, organic silts, and shells in beach sands, while horizontal and vertical error bars indicate chronological and RSL uncertainties, respectively. The highlighted interval indicates the concentration of the highest RSL estimates between approximately 7.1 and 6.0 cal ka BP, with values of about 1.0–2.6 m above present. Toward 6.0–5.0 cal ka BP, the distribution of the SLIPs shows an increasing representation at lower RSL elevations, illustrating the beginning of the subsequent decline.

where original depositional context can be demonstrated and later erosion or reworking appears limited. Although beachrock generally has a broader indicative range than microatolls, its intertidal origin makes it a useful marker for mid- to late Holocene shoreline position. In contrast, shell-bearing deposits and organic silts display wider scatter in inferred RSL and much larger combined uncertainty. These lower-confidence records provide broader supporting constraints but, because of their larger uncertainties, do not independently constrain the amplitude of the mid-Holocene highstand.

4.4. Modeled Holocene RSL change

The EIV-IGP reconstruction identifies three distinct phases of Holocene RSL change in the northern SCS (Fig. 4a, b). The early Holocene transgression was characterized by markedly non-uniform rates of RSL rise. From approximately 9.5 to 8.6 cal ka BP, RSL rose from ∼−25 m to ∼−8 m, corresponding to a mean RSL rise rate of ∼19 mm/yr (Fig. S1). Thereafter, from approximately 8.6 to 7.0 cal ka BP, RSL rose more slowly from ∼−8 m to ∼+1.8 m, at a mean RSL rise rate of ∼6 mm/yr. This contrast indicates an interval of accelerated RSL rise around 9 cal ka BP, followed by a deceleration toward the mid-Holocene highstand. Because the early Holocene reconstruction is constrained by relatively sparse and lower-precision records, these segment rates should be regarded as first-order estimates rather than as evidence for a precisely resolved short-lived event.

During the mid-Holocene highstand from 7.0 to 3.4 cal ka BP, RSL remained persistently above present and reached a peak elevation of ∼2.2 m at ∼6.6 cal ka BP. The best-constrained range of highstand elevation is 1.4–2.6 m. We define 3.4 cal ka BP as the end of the principal highstand phase, as indicated by a clear reduction in the rate of RSL fall, rather than a return to modern sea level.

During the late Holocene from 3.4 cal ka BP to the present, RSL gradually declined from ∼1.0 m toward the modern datum, with centennial-scale fluctuations superimposed on the long-term falling trend.

Posterior uncertainty band width exhibits a significant negative correlation with local SLIP density and proxy precision (Spearman's $\rho = -0.937$, circular-shift $p = 0.011$). Constraints are tightest across the densely sampled mid-Holocene interval. Fig. 4b further visualizes the temporal evolution of Holocene RSL change rates. Positive values represent RSL rise, whereas negative values represent RSL fall. The rate envelope indicates rapid RSL rise during the early Holocene, with the highest rates occurring between 9.5 and 8.6 cal ka BP (approximately 19 mm/yr) and lower but still positive rates between 8.6 and 7.0 cal ka BP (approximately 6 mm/yr). Rates approached zero during the 7.0–3.4 cal ka BP mid-Holocene highstand and became weakly negative after 3.4 cal ka BP, consistent with the three-stage RSL evolution described above.

RSL first reached and exceeded the modern datum at approximately 7.4 cal ka BP and attained a maximum of about 2.2 m above present at approximately 6.6 cal ka BP. Thereafter, the reconstruction shows a general but fluctuating decline rather than an abrupt termination of the

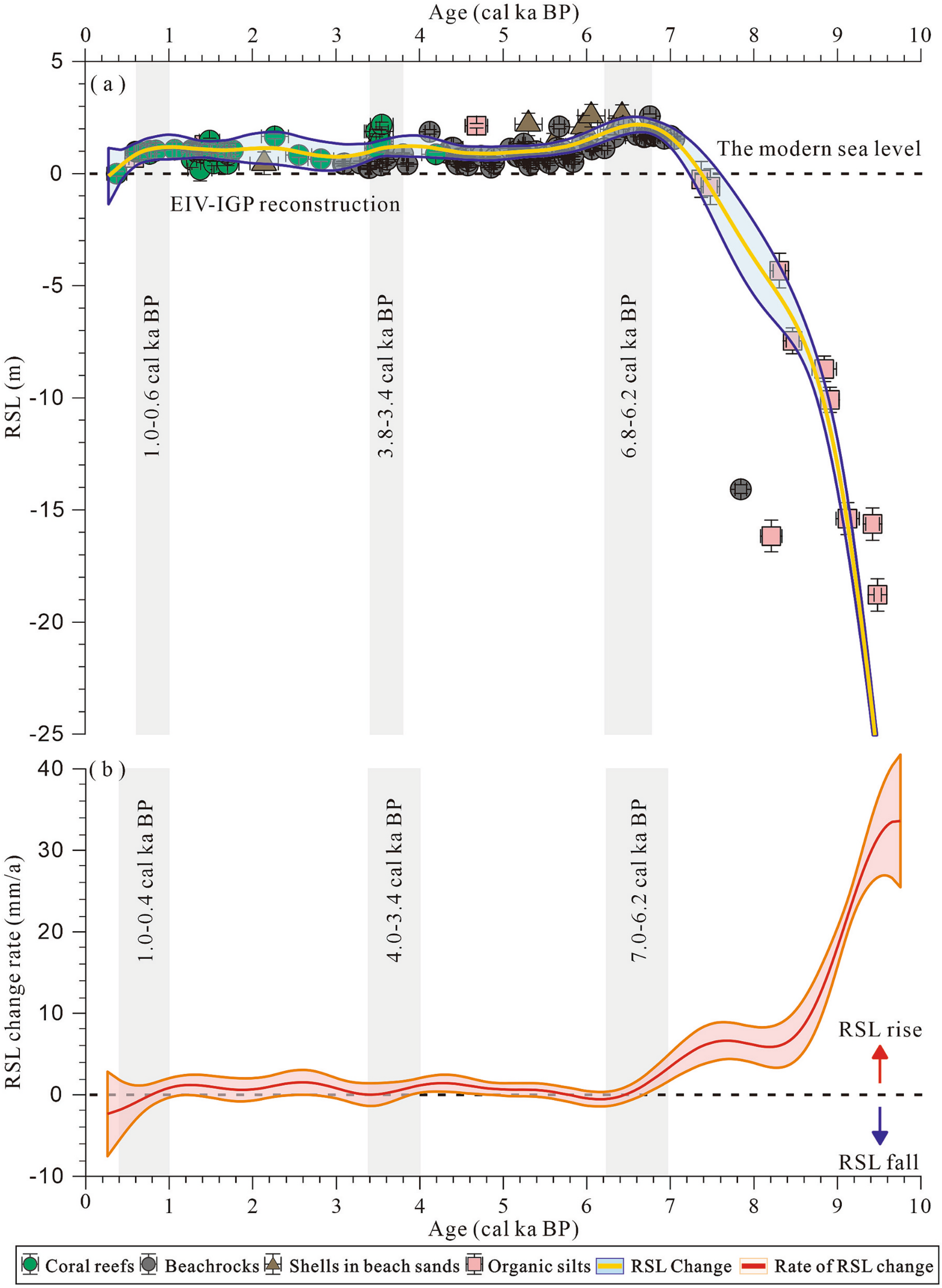

Fig. 4. Reconstruction of Holocene RSL change in the northern SCS using the EIV-IGP model. (a) Reconstructed RSL history together with the screened SLIPs used to constrain the reconstruction. Different symbols and colors distinguish the principal proxy classes, including coral reefs, beachrock, shell-bearing deposits, and organic silts. Horizontal and vertical error bars show the associated chronological and RSL uncertainties of the observations. The dashed horizontal line marks modern sea level. The reconstructed RSL curve and its associated uncertainty envelope show the temporal evolution of RSL inferred from the screened dataset. Gray vertical bands and annotations highlight selected intervals discussed in the text. (b) Reconstructed rate of RSL change through the Holocene. Positive values indicate RSL rise and negative values indicate RSL fall, with the dashed horizontal line representing zero RSL change. The associated envelope represents uncertainty in the reconstructed rate. Gray vertical bands and annotations highlight key transition and peak intervals discussed in the text.

highstand. We use approximately 3.4 cal ka BP as an operational boundary between the principal elevated-RSL phase and the subsequent lower-amplitude late-Holocene fluctuations, because the modeled rate curve indicates a marked reduction in the magnitude of RSL fall around this time. This boundary does not indicate that RSL had returned to the modern datum: RSL remained approximately 0.8–1.0 m above present during parts of the subsequent interval before finally converging toward the modern sea level.

Similar distinctions between the termination of a principal highstand phase and the later return to present sea level have been reported from other far-field sites in Southeast Asia. In southeastern Vietnam, the principal highstand was dated to 6.7–5.0 cal ka BP, although RSL remained above present and continued to fall gradually until the late Holocene (Stattegger et al., 2013). Comparable prolonged post-highstand falls have also been reconstructed from the Malay Peninsula (Zhang et al., 2021). Such behavior is consistent with a gradual far-field RSL fall driven partly by GIA-related continental levering and equatorial ocean siphoning (Mitrovica and Milne, 2002).

The uncertainty envelope is narrowest during the densely sampled mid-Holocene elevated phase (3.4–7.0 cal ka BP), with a median half-width of about 0.337 m. In contrast, the half-width increases to 0.552 m during 0.3–3.4 cal ka BP, and reaches 1.3 m or more in the early Holocene intervals (see Supplementary Analyses Section 2.3; Tables S3–S4).

This temporal pattern reflects the composition and precision of the retained dataset. Of the 146 SLIPs used in the reconstruction, 87 (59.6%) are coral indicators. Coral SLIPs have a median vertical uncertainty of 0.098 m and a median chronological uncertainty of 17 yr at 1σ, compared with median vertical uncertainties of 0.350 m for beachrock, 0.500 m for shells, and 0.650 m for organic silts. Proxy groups differ significantly in both vertical and chronological uncertainty (Kruskal–Wallis tests, $p < 0.001$). Coral uncertainties are also significantly smaller than those of the combined non-coral dataset (Mann–Whitney tests, $p < 0.001$).

The concentration of high-precision observations is greatest during 3.4–7.0 cal ka BP, which contains 95 SLIPs, including 81 coral indicators (85.3%). Median input uncertainties in this interval are 0.098 m vertically and 19 yr chronologically at 1σ. Across the reconstruction, the plotted uncertainty half-width is strongly negatively associated with the number of SLIPs within ±0.5 kyr (Spearman $\rho = -0.937$, circular-shift $p = 0.011$) and strongly positively associated with the local inverse-variance effective vertical uncertainty ($\rho = 0.934$, $p = 0.011$). The narrow mid-Holocene envelope is quantitatively associated with high data density and the dominance of precise coral SLIPs rather than to an assumption of error-free observations.

4.5. Comparison with GIA predictions and regional offsets

Compared with GIA predictions, the geological records from all three subregions plot predominantly below the modeled far-field RSL curves (Fig. 5), and the magnitude of model-data residuals varies spatially. For Hainan Island (Fig. 5a) and Leizhou Peninsula (Fig. 5b), the median mid-Holocene residuals are about 0.5–1.0 m and are compatible with modest long-term vertical land motion and proxy uncertainty. In contrast, the Pearl River Delta (Fig. 5c) shows much larger residuals, commonly 1.5–2.5 m during the mid-Holocene, which may reflect contributions from sediment compaction, accommodation-space evolution, and local vertical land motion.

The positive mid-Holocene highstand signal remains robust in all subregions when only high-confidence coral and beachrock records are considered, indicating that it is not an artefact of compaction-prone lowland deposits.

5. Discussion

5.1. The strongest evidence for a mid-Holocene highstand comes from coral and beachrock records

A central debate in northern SCS RSL research is whether a distinct mid-Holocene highstand existed above present sea level. Our results show that the interpretation depends strongly on proxy quality. When all published records are treated equally, the highstand signal is obscured by considerable scatter. In contrast, the signal becomes much clearer when the analysis is restricted to in situ corals and stratigraphically secure beachrock.

The most persuasive evidence comes from in situ coral reefs, especially *Porites* microatolls, and from well-preserved beachrock. Coral microatolls are especially valuable because their growth geometry

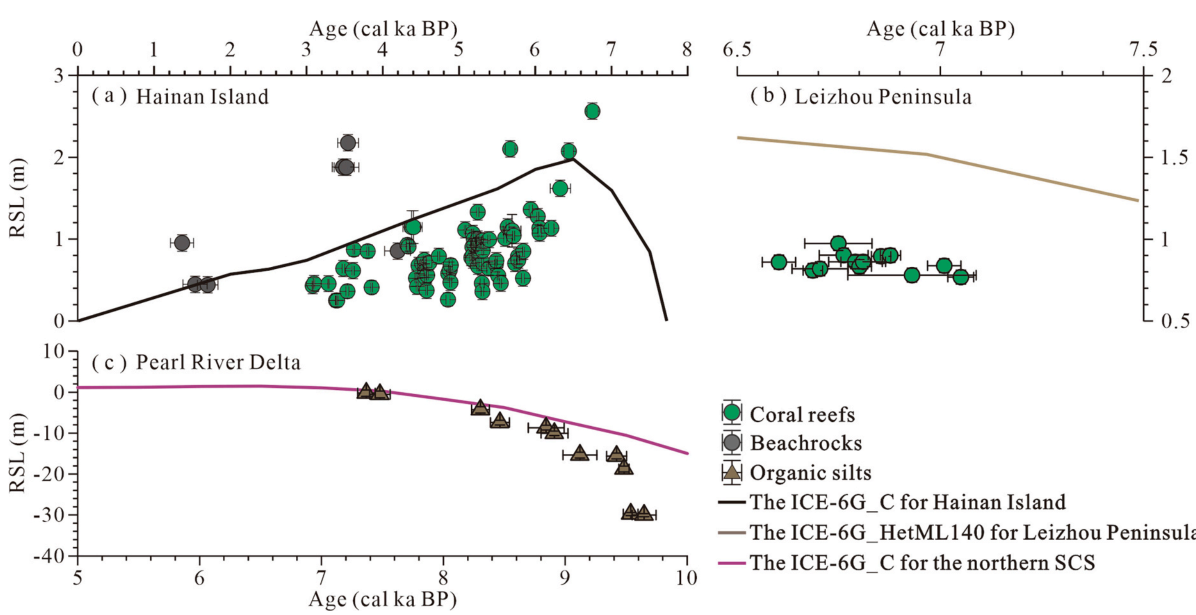

Fig. 5. Comparison between geological SLIPs and GIA-predicted RSL curves for representative northern SCS sectors: (a) Hainan Island; (b) Leizhou Peninsula; and (c) Pearl River Delta. The residuals between the measured points and the GIA curves are interpreted as composite offsets that may include vertical land motion, sediment compaction, datum uncertainty, proxy uncertainty, and GIA-model uncertainty. They should not be attributed solely to tectonic subsidence unless independently constrained.

records a biologically meaningful upper limit that can be tied closely to local tidal levels. When combined with U-Th dating and high-precision elevation surveying, they can yield RSL constraints with comparatively narrow vertical and chronological uncertainty (Yue et al., 2024, 2025; Tang and Yue, 2023; Yu and Chen, 2009). In the eastern Hainan and Leizhou sectors, multiple coral records independently indicate RSL above the modern datum during the mid-Holocene. Beachrock records from Guangdong, Hainan, and Weizhou Island broadly reinforce this conclusion by indicating former intertidal positions above the present shoreline during parts of the mid-to-late Holocene (Yan et al., 2021; Tang and Yue, 2023).

By contrast, shells and organic silts alone do not provide equally strong evidence. They often yield useful broad constraints on marine transgression, shoreline proximity, or marginal-marine conditions, but their indicative ranges are wider and their post-depositional histories more uncertain. Shells may be reworked or transported, and organic silts are vulnerable to compaction, bioturbation, and changes in accommodation space that complicate their relationship to former RSL (Zong, 2004). For this reason, the regional highstand interpretation should be based primarily on coral- and beachrock-dominated evidence, with lower-confidence sedimentary indicators used as contextual support rather than as leading constraints.

The distinction among proxy types also affects the geological interpretation of the reconstructed RSL history. After restricting the analysis to the most reliable coral and beachrock indicators, the mid-Holocene highstand emerges as a coherent regional signal that is less sensitive to the inclusion of low-confidence sedimentary records. The quality-screened database therefore provides strong support for a regional mid-Holocene RSL highstand above present sea level, although the magnitude of the highstand may vary among individual coastal sectors.

5.2. Why previous studies reached different conclusions: data compilation, proxy quality, and modelling

Differences among published northern SCS RSL reconstructions can arise from three main methodological sources. First, inconsistent metadata standards, age calibration schemes and undifferentiated SLIP/limiting data classification generate incomparable raw datasets (Hijma et al., 2025; Mann et al., 2019; Shennan et al., 2002). Second, some earlier regional syntheses did not explicitly distinguish among proxies with substantially different tidal bandwidth, reworking risk, compaction susceptibility and dating precision (Engelhart and Horton, 2012; Zong, 2004). Third, deterministic curve-fitting approaches do not necessarily propagate chronological and vertical uncertainties as explicitly as the EIV-IGP probabilistic framework, which incorporates these uncertainties probabilistically throughout the reconstruction (Cahill et al., 2015; Khan et al., 2015). These three categories are related, but they occur at different stages and require different methodological solutions.

The present study addresses these problems by applying an explicit screening strategy (see Supplementary Analyses Section 2.3–2.4; Tables S3, S5). This approach does not eliminate all uncertainty, nor does it prove that every sector of the northern SCS experienced identical highstand magnitudes. It does, however, render data-inclusion logic transparent and reduces the probability that weakly constrained records dominate the regional interpretation. The highstand signal retained after screening is therefore best understood as a robust regional tendency expressed most clearly in coral- and beachrock-bearing sectors. Methodologically, this is achieved through three interconnected operations: harmonization of the database using consistent metadata standards, proxy-specific quality screening, and explicit propagation of age and elevation uncertainties within the EIV-IGP probabilistic framework.

5.3. Regional vertical offsets: tectonic subsidence, sediment compaction, and model-data residuals

Comparison with GIA predictions indicates that northern SCS RSL broadly follows expected far-field postglacial behavior, but the residuals record composite offsets rather than tectonic motion alone. This caveat is especially important in compaction-prone deltaic settings such as the Pearl River Delta, where organic-rich and muddy deposits may have experienced substantial post-depositional lowering.

Tectonic processes nevertheless remain relevant. The northern margin of the SCS has a long history of post-rift tectonic deformation (Briais et al., 1993), while late-Quaternary differential uplift and subsidence have also been documented along parts of the northern SCS coast (Pedoja et al., 2008; Tang et al., 2011). In this context, modest residuals in Hainan Island and the Leizhou Peninsula may reflect a combination of slow tectonic subsidence and unmodeled local effects, while the much larger residuals in the Pearl River Delta are consistent with contributions from both tectonic subsidence and sediment compaction.

Model-data residuals should therefore be treated as diagnostic clues rather than direct corrections. Applying a uniform tectonic correction to every SLIP would imply a level of precision that is not supported by the available geodetic, stratigraphic and geotechnical constraints, which vary substantially across the region. We therefore place greater weight on coral and beachrock records from sectors with limited evidence of vertical displacement. Lowland sedimentary records are treated as lower-confidence constraints. Model-data residuals are interpreted as reflecting several possible contributions, including GIA uncertainty, compaction, datum error, proxy uncertainty, and vertical land motion.

The rapid early Holocene rise inferred for the northern SCS occurred during the final major phase of postglacial ice-sheet decay. A probabilistic synthesis of far-field records estimated rates of approximately 13–15 mm/yr around 9.5 cal ka BP (Stanford et al., 2011), while the global reconstruction of Lambeck et al. (2014) indicates that the main deglacial rise continued until approximately 8.2 cal ka BP before progressively slowing. The magnitude and timing of the northern SCS reconstruction are therefore compatible with this broader deglacial context. However, regional records require additional caution. On the southern Vietnam shelf, Tjallingii et al. (2010, 2014) identified rapid flooding between approximately 9.5 and 8.2 cal ka BP, but attributed a substantial part of the regional RSL offset to differential hydro-isostatic adjustment and shelf topography rather than to eustatic rise alone. Moreover, estimates of the near-instantaneous eustatic contribution associated specifically with the 8.2 ka event are substantially smaller than the total regional rise, probably less than approximately 1.2 m (Törnqvist et al., 2004).

We therefore interpret the northern SCS acceleration as temporally consistent with the interval commonly associated with Meltwater Pulse 1C (MWP-1C). The temporal correspondence alone does not provide independent evidence for a discrete 20-m global meltwater pulse. The reconstructed regional signal likely combines continued ice-volume loss, GIA and hydro-isostatic effects. Rapid landward shoreline migration across the low-gradient shelf and local vertical displacement may also have contributed. The interpretation is further limited by the sparse early Holocene dataset.

5.4. Hydroclimatic context: what climate can and cannot explain

The reconstructed Holocene RSL trajectory is more consistent with the expected effects of global ice volume change and far-field GIA than with a dominant control by regional hydroclimatic variability. Quantitative statistical analysis finds no significant association between millennial-scale RSL change and any of the selected regional climate records, as detailed below and Supplementary Analyses Section 2.5 (Table S6).

This does not mean that climate variability has no influence on the sea-level archive. Monsoon-driven changes in precipitation, runoff and sediment supply may have altered the depositional context of sedimentary proxies (Fu et al., 2020; He et al., 2024; Zhang et al., 2023), whereas SST and water clarity can influence coral growth and reef development (Ma et al., 2021; Carricart-Ganivet, 2004; Lough and Barnes, 2000). These archive-modulating effects are distinct from a first-order control on meter-scale millennial RSL magnitude.

For the mid-Holocene, Stattegger et al. (2013) reconstructed RSL rise from approximately −4 m at 8.0 cal ka BP to +1 m at 6.9 cal ka BP along the southeastern Vietnamese coast, followed by a highstand of approximately +1.4 to +1.6 m between 6.7 and 5.0 cal ka BP and a maximum near 6.0 cal ka BP. After 5.0 cal ka BP, RSL declined gradually at approximately 0.25 mm/yr but remained above present until the late Holocene. The northern SCS reconstruction shows a broadly similar timing of the highstand maximum and a comparable prolonged post-highstand decline, although the reconstructed peak is higher and the highstand phase persists longer.

These similarities indicate a regionally coherent transition from rapid early Holocene transgression to a mid-Holocene highstand and subsequent gradual decline. Differences in highstand magnitude and duration may reflect spatially variable GIA and hydro-isostatic adjustment, continental-shelf geometry, local vertical land motion, proxy interpretation and differences in the density and precision of the available SLIPs.

The broad timing of the reconstructed early Holocene rise and mid-Holocene highstand is consistent with postglacial GMSL behavior and far-field hydro-isostatic adjustment. Stronger summer monsoon conditions during the early to mid-Holocene likely enhanced precipitation and freshwater discharge, while changes in riverine sediment supply influenced coastal depositional environments (He et al., 2024; Yin et al., 2021; Fu et al., 2020). Similarly, warm mid-Holocene conditions may have favored reef growth and improved the preservation of coral-based indicators in some settings (Ma et al., 2021). These relationships are geologically meaningful, but they should not be mistaken for evidence that monsoon or SST variations were the primary control on meter-scale RSL magnitude.

Fig. 6 shows that the reconstructed RSL curve and the selected climate records exhibit distinct long-term trends and shorter-term fluctuations through the Holocene. RSL rose rapidly during the early Holocene, reached and exceeded the modern datum at approximately 7.4 cal ka BP, and attained a maximum of about +2.2 m at approximately 6.6 cal ka BP, after which it underwent a general but fluctuating decline toward the present sea level (Fig. 6a). Northern SCS SST varied within a comparatively narrow range, with repeated centennial- to millennial-scale excursions rather than a simple monotonic trend (Fig. 6b, Wu et al., 2017). El Niño–Southern Oscillation (ENSO) variability was generally weaker during much of the early to mid-Holocene and became stronger and more variable toward the late Holocene (Fig. 6c, Liu et al., 2014). Mean annual precipitation and temperature broadly increased toward the mid-Holocene and subsequently declined, although both records contain substantial shorter-term variability (Fig. 6d, e, Zhang et al., 2023). Dongge Cave $\delta^{18}O$ values generally became less negative toward the Late Holocene, consistent with a long-term weakening of the East Asian summer monsoon, while Northern Hemisphere summer insolation declined progressively from the early Holocene toward the present (Fig. 6f, g, Berger and Loutre, 1991; Wang et al., 2005). These records therefore document substantial changes in the environmental setting of the northern SCS, but the timing of their trends and shorter-term fluctuations is not consistently aligned with the reconstructed RSL trajectory.

We tested the statistical robustness of the visual correspondences shown in Fig. 6. To do so, we compared the reconstructed RSL history with each climate record using first-difference Spearman correlations, while accounting for temporal autocorrelation via randomization and applying false-discovery-rate correction (see Supplementary Analyses Section 2.5 and Table S6 for details). Lagged correlations up to ±0.6 kyr were also examined. No statistically significant association was detected between RSL change and northern SCS SST, ENSO variability, mean annual precipitation, mean annual temperature, Dongge Cave $\delta^{18}O$, or Northern Hemisphere summer insolation. The first-difference Spearman coefficients ranged from −0.027 to 0.341, with all adjusted q values ≥0.875. Allowing chronological lags of up to ±0.6 kyr likewise produced no significant association, with all adjusted q values ≥0.60.

These results indicate that the broad visual correspondences in Fig. 6 do not provide statistically robust evidence that Holocene climate variability directly controlled millennial-scale RSL change. However, the absence of a detectable association should not be interpreted as proof that climatic conditions had no influence on coastal environments (Haam and Huybers, 2010; Hu et al., 2017). The present analysis evaluates temporal association rather than causal effects and is limited by the temporal resolution, chronological uncertainty, and number of effectively independent observations in the records.

ENSO, SST, and monsoon variability nevertheless remain relevant to the environmental setting in which the SLIPs formed and were preserved. Paleoclimate studies indicate that tropical Pacific variability changed substantially through the Holocene (Chen et al., 2024; Liu et al., 2014). Such variability may have influenced the hydroclimatic environment in which coastal proxies formed and were preserved. Previous process-based studies also suggest that precipitation and river discharge may influence sediment supply and coastal depositional environments, whereas SST, water clarity, and ecological conditions may affect reef growth and carbonate preservation (Yue et al., 2024; Carricart-Ganivet, 2004; Lough and Barnes, 2000). These potential pathways were not quantified as causal effects in the present study. Fig. 6 is therefore retained to illustrate environmental and archive-forming context rather than as evidence of direct climatic forcing of RSL. The long-term RSL trajectory is broadly consistent with the expected effects of ice-volume change and GIA. Hydro-isostatic adjustment, vertical land motion, and sediment compaction may also contribute, but their individual effects cannot be separated with the present dataset.

5.5. Comparison with other far-field regions in the western Pacific and beyond

The northern SCS record should be considered within the wider pattern of far-field tropical and subtropical mid-Holocene highstands. Comparable higher-than-present RSL has been reported from the Malay Peninsula, parts of Japan and other Indo-Pacific margins (Chiba et al., 2016; Parham et al., 2014; Zhang et al., 2021). These broadly synchronous highstands are commonly attributed to far-field GIA processes, particularly continental levering and equatorial ocean siphoning, with additional effects from rotational feedback (Bradley et al., 2016; Mitrovica and Milne, 2002).

Quantitatively, the magnitude of the mid-Holocene highstand shows clear spatial variation across the region (Fig. 7). The 1.4–2.6 m range reconstructed in this study is slightly higher than the 1.0–1.5 m highstand reported from the east coast of the Malay Peninsula (Zhang et al., 2021), and broadly comparable to the 1.4–1.6 m peak recorded along the southeastern Vietnamese coast (Stattegger et al., 2013). When compared with GIA-predicted curves from further north along the East Asian coast, our reconstructed highstand magnitude falls between the predictions for Hangzhou Bay and the Leizhou Peninsula (Fig. 7a), consistent with the expected latitudinal gradient of far-field GIA effects.

Fig. 7b directly compares screened SLIP datasets and reconstructed mid-to-late Holocene RSL trajectories between the northern SCS and the east Malay Peninsula. The two regions share a consistent evolutionary pattern: rapid early-Holocene transgression, a sustained mid-Holocene highstand, and gradual late-Holocene sea-level decline. However, our northern SCS reconstruction yields a higher peak RSL range (1.4–2.6 m) relative to the Malay Peninsula's 1.0–1.5 m highstand, a discrepancy driven by combined latitudinal GIA gradients, local vertical land motion, and differences in proxy data density and precision between the two study areas.

This spatial variability reflects two geological processes and differences in proxy quality. GIA processes generate inherently heterogeneous

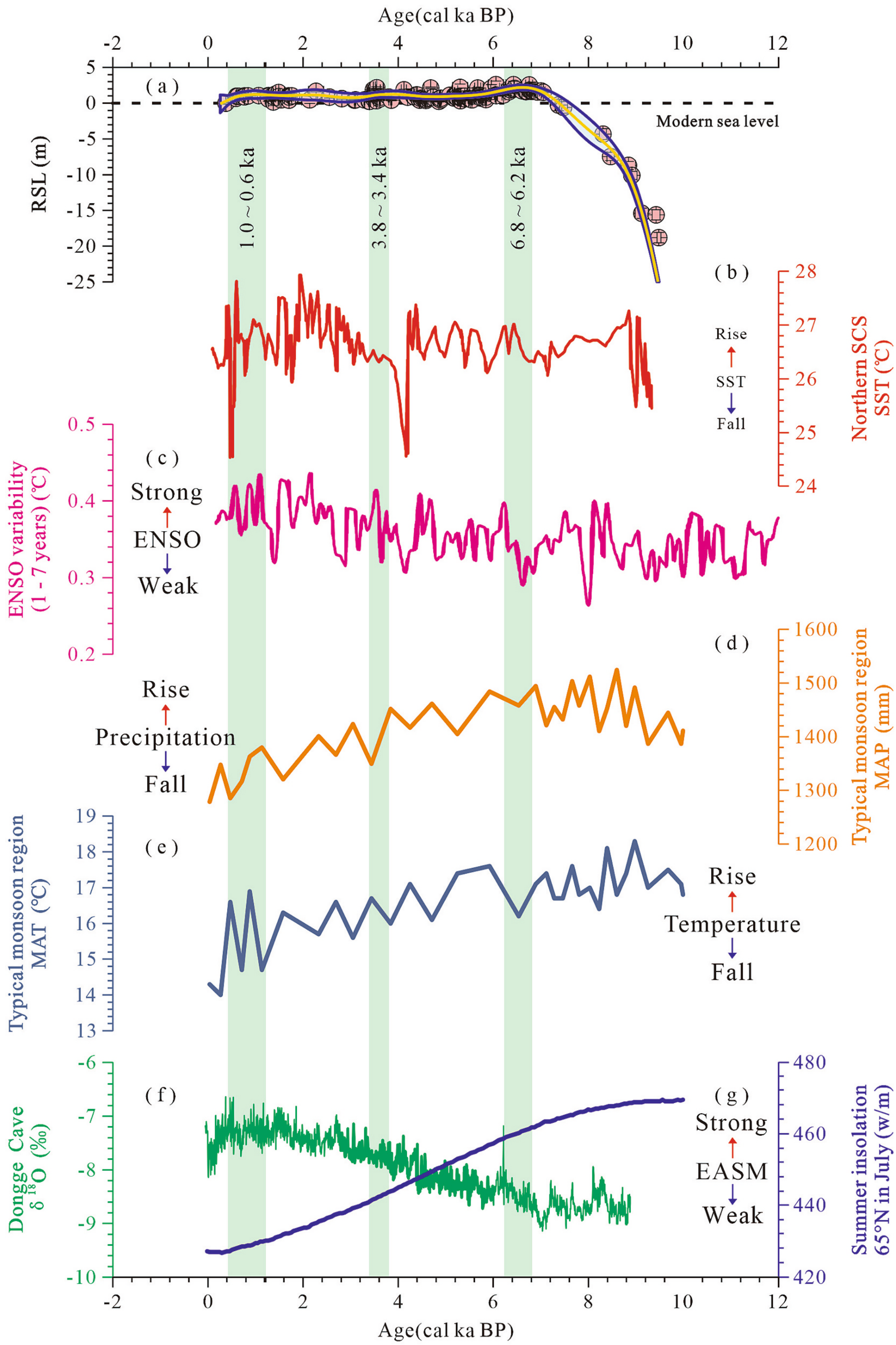

Fig. 6. Comparison between the reconstructed northern SCS RSL curve and selected Holocene climate records. From top to bottom: RSL reconstruction from this study; northern SCS SST variations (Wu et al., 2017); ENSO amplitude expressed as the standard deviation of Niño 3.4 interannual SST variability (Liu et al., 2014); pollen-derived mean annual precipitation and temperature for the Asian monsoon region (Zhang et al., 2023); Dongge Cave stalagmite $\delta^{18}O$ (Wang et al., 2005); and Northern Hemisphere summer insolation (Berger and Loutre, 1991). The comparison is intended to evaluate temporal correspondence and archive context, not to assign climate variables as first-order drivers of millennial-scale RSL magnitude. First-difference Spearman correlation analysis confirms no significant association between RSL change and any individual climate record (see Section 5.4 and Supplementary Analyses Section 2.5 for details). The climate records are therefore shown as environmental and archive-forming context rather than as evidence of direct climatic control on millennial-scale RSL magnitude.

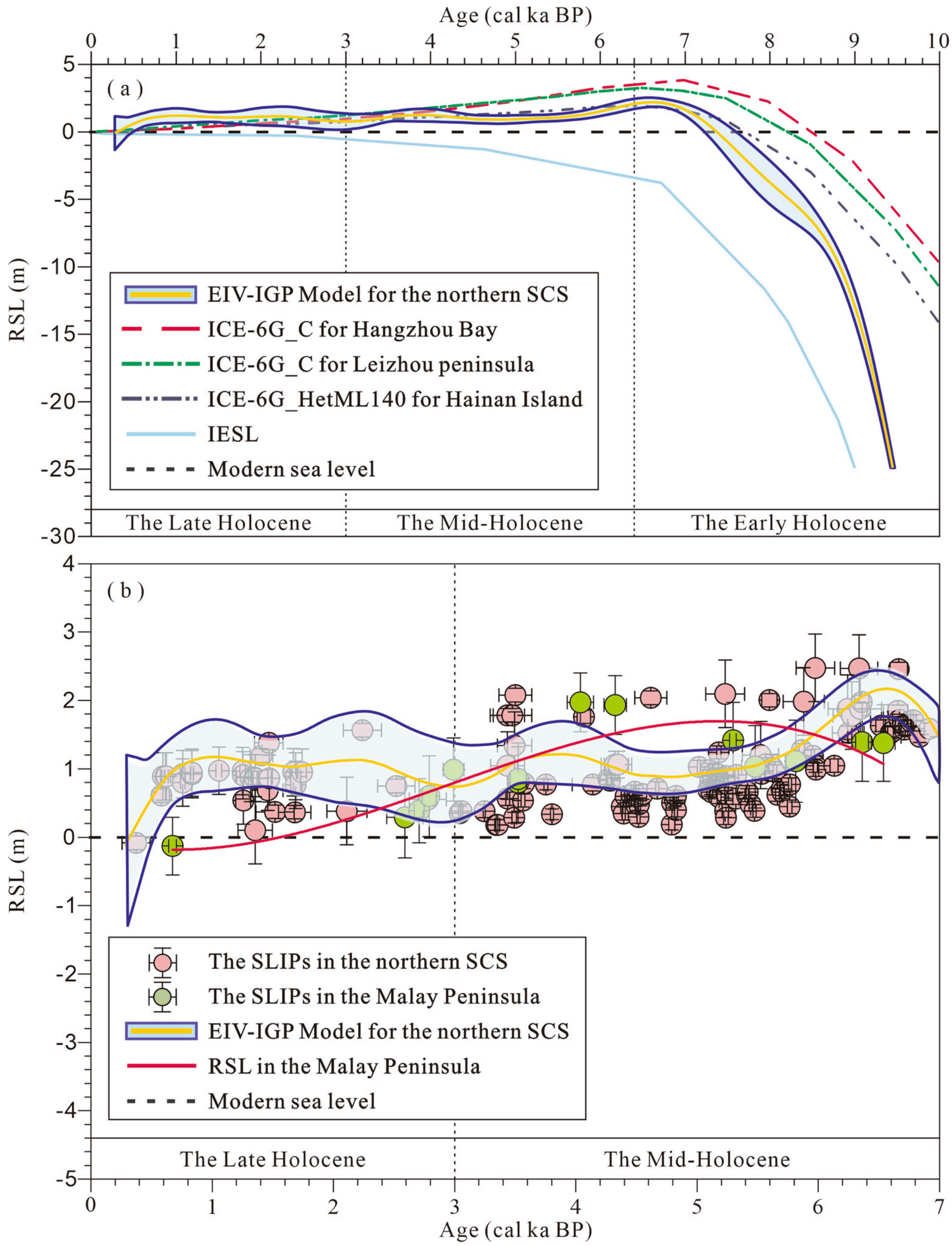

Fig. 7. Comparison of Holocene RSL among different regions. (a) RSL change curves for the northern SCS and selected comparison regions, together with the ice-equivalent sea-level curve of Lambeck et al. (2014). The Leizhou Peninsula, Hainan Island, and Hangzhou Bay curves are based on GIA predictions, whereas the northern SCS curve is derived from the EIV-IGP reconstruction. (b) Comparison of measured SLIPs and reconstructed RSL changes from the northern SCS and the Malay Peninsula (Zhang et al., 2021).

far-field responses, because sites at different distances from former ice sheets and with different upper-mantle viscosity structures experience different magnitudes of continental levering and ocean siphoning. This regional heterogeneity is also evident in the contrasting Holocene RSL responses of Hangzhou Bay and the Sundaland region (Xiong et al., 2020). Local vertical land motion further modulates the recorded RSL signal: tectonically stable, rocky, and reef-fringed coasts such as Hainan Island show a more clearly expressed highstand that is broadly consistent with far-field GIA predictions, whereas subsiding deltaic plains such as the Pearl River Delta tend to yield systematically lower RSL estimates because of sediment compaction and tectonic subsidence (Tang et al., 2011; Xiong et al., 2018). Proxy type and data quality introduce additional systematic biases. Some earlier regional syntheses incorporated substantial numbers of compaction-prone muddy and shell deposits, which may bias reconstructed RSL elevations downward. By contrast, our quality-screened dataset, weighted toward in situ coral and well-preserved beachrock indicators, provides tighter constraints on the upper range of the regional highstand.

The regional comparison also highlights the value of coral and beachrock as comparable sea-level indicators across tropical coastlines. Because these SLIPs have well-constrained indicative meanings and are less affected by post-depositional alteration than estuarine muds or marsh deposits, they provide a more robust basis for testing the spatial variability of far-field RSL behavior. The northern SCS therefore provides an additional constraint on the western Pacific Holocene RSL archive and a regional benchmark for evaluating GIA and ice sheet history models.

The comparatively narrow mid-Holocene uncertainty envelope should be interpreted as high conditional posterior precision rather than uniform absolute accuracy. Published EIV-IGP applications show that uncertainty varies strongly with the number, temporal distribution, and proxy-specific uncertainty of the available SLIPs. In Singapore, where 93% of the SLIPs occur between 9.5 and 5.6 cal ka BP and only seven SLIPs constrain the late Holocene, the reconstruction yielded a mid-Holocene highstand of 4.0 ± 4.5 m and a late-Holocene estimate of −2.4 ± 2.8 m (Chua et al., 2021).

Along the Atlantic coast of Africa, EIV-IGP 1σ uncertainties vary substantially among regions and intervals. Examples near 7 cal ka BP include approximately ±0.7 m in Senegal and the northern Gulf of Guinea and ± 2.0 m in Congo, while reconstructed highstand uncertainties range from approximately ±0.8 to ±2.4 m. The authors explicitly noted that reconstruction accuracy depends on the number of SLIPs and their chronological and vertical uncertainties (Vacchi et al., 2025).

Sub-metre precision is therefore not unprecedented when datasets are dense and internally coherent. For Pohnpei and Kosrae, an EIV-IGP reconstruction based on 68 SLIPs from 15 sites estimated a total late-Holocene RSL rise of 4.3 ± 0.4 m at 1σ (Sefton et al., 2022). The northern SCS uncertainty is of a similar order but arises from a different proxy structure: 85.3% of the records during the principal elevated-RSL phase are coral SLIPs with a median vertical uncertainty of 0.098 m. Thus, the northern SCS reconstruction is unusually precise relative to sediment-dominated or data-sparse regional records, but its precision is consistent with other densely sampled EIV-IGP applications.

These comparisons are descriptive rather than a formal cross-study significance test because the published studies report different uncertainty summaries, time intervals, proxy assemblages, and credible-interval conventions. A valid pooled hypothesis test would require the posterior draws from all reconstructions on a common prediction grid. The statistical justification for the northern SCS precision is therefore based on the proxy-group tests and uncertainty–data-density analysis within the present dataset.

5.6. Implications, limitations, and priorities for future work

Several limitations remain despite the improved database and clearer constraints on the mid-Holocene highstand. These limitations also identify priorities for future work.

The compiled dataset displays obvious spatiotemporal imbalance. Pre-8 cal ka archives are extremely limited across the full study domain, and the Beibu Gulf coastline lacks high-precision coral SLIPs to support independent subregional RSL modelling. Future field investigations targeting these data-poor areas, combined with RTK-GNSS topographic measurement and high-resolution U-series dating, could improve early-Holocene constraints and reduce reconstruction uncertainty for the transgressive stage.

Beyond uneven data distribution, we are unable to numerically separate individual drivers of model-data residuals. Current analysis only qualitatively attributes mismatches between reconstructed curves and ICE-6G predictions to combined signals of sediment compaction, vertical tectonic motion and GIA structural error; without paired sediment core stratigraphy and geotechnical compaction tests, alongside long-term geodetic monitoring records, we cannot quantify the respective weight of each offset component. Future delta-focused field work can address this ambiguity by integrating multi-proxy stratigraphic observation with laboratory compaction measurements.

Future work should compare several GIA models with different mantle-viscosity structures and ice histories. This would provide a more direct estimate of model uncertainty than reliance on the ICE-6G series alone.

6. Conclusions

This study presents a quality-screened Holocene sea-level index-point (SLIP) database for the northern South China Sea, comprising 374 compiled records and 146 records retained for probabilistic reconstruction. The screening framework distinguishes high-confidence coral and beachrock indicators from lower-confidence sedimentary records and explicitly incorporates chronological and vertical uncertainties. This approach provides a more consistent basis for reconstructing regional Holocene RSL variability and evaluating differences among previous reconstructions.

Proxy quality is a critical control on the resolution of Holocene RSL reconstruction. In situ corals and intact beachrock provide substantially tighter vertical constraints than shells and organic-rich sediments, highlighting the importance of screening proxy reliability when synthesizing heterogeneous geological records. This contrast may help explain differences among previous regional reconstructions and demonstrates the value of a quality-controlled database for resolving the regional RSL signal.

The screened dataset reveals a regionally coherent mid-Holocene highstand between 7.0 and 3.4 cal ka BP, with maximum reconstructed RSL elevations of approximately 1.4–2.6 m above present sea level. The highstand remains evident when the reconstruction is restricted to coral and beachrock records, indicating that the signal cannot be attributed solely to compaction-prone deltaic sediments. The results therefore provide strong geological support for a mid-Holocene highstand in the northern South China Sea.

Comparison with ICE-6G GIA predictions further indicates that the residuals between geological observations and model predictions are spatially variable and may reflect a combination of vertical land motion, sediment compaction, proxy and datum uncertainty, and GIA-model uncertainty. The larger residuals in the Pearl River Delta are consistent with greater contributions from sediment compaction and vertical land motion, whereas the smaller residuals on Hainan Island and the Leizhou Peninsula indicate smaller overall model–data offsets.

Statistical analyses further reveal no significant millennial-scale relationship between RSL variability and SST, ENSO, monsoon precipitation, Dongge Cave $\delta^{18}O$, or Northern Hemisphere summer insolation. These results indicate that hydroclimatic variability may influence coral growth, sediment delivery, and proxy preservation, but no statistically significant temporal association was detected between the selected hydroclimatic records and millennial-scale RSL variability.

Overall, the reconstructed RSL history supports the characteristic far-field western Pacific sequence of early-Holocene transgression, a mid-Holocene highstand, and subsequent late-Holocene sea-level fall. By combining systematic proxy screening with a probabilistic RSL reconstruction, this study provides a more robust geological constraint on Holocene sea-level evolution in the northern SCS and offers a quality-controlled dataset for evaluating and refining regional GIA models and Holocene ice-sheet histories.

CRediT authorship contribution statement

Yuanfu Yue: Writing – review & editing, Writing – original draft, Supervision, Methodology, Funding acquisition, Data curation, Conceptualization. **Bo Zhang:** Writing – review & editing, Visualization, Methodology. **Lichao Tang:** Writing – review & editing, Writing – original draft, Validation, Methodology. **Yiheng Zhao:** Writing – review & editing, Visualization, Methodology. **Jie Wang:** Validation, Methodology. **Ruizhe Yang:** Validation, Methodology.

Declaration of competing interest

The authors declare that they have no known competing financial interests or personal relationships that could have appeared to influence the work reported in this paper.

Acknowledgments

This work was supported by the National Natural Science Foundation of China (42366002), and the Guangxi Scientific Projects (2025GXNSFAA069160). We sincerely thank Prof. Haixian Xiong of Sun Yat-sen University and Dr. Tanghua Li of City University of Hong Kong for the GIA model data and professional guidance provided for this article.

Appendix A. Supplementary data

Supplementary data to this article can be found online at https://doi.org/10.1016/j.palaeo.2026.114210.

Data availability

The authors confirm that all data necessary to support the scientific findings of this paper have been provided.

References

An, Z., 2000. The history and variability of the East Asian paleomonsoon climate. Quat. Sci. Rev. 19, 171–187.
Berger, A., Loutre, M.F., 1991. Insolation values for the climate of the last 10 million years. Quat. Sci. Rev. 10, 297–317.
Bradley, S.L., Milne, G.A., Horton, B.P., Zong, Y.Q., 2016. Modelling sea level data from China and Malay-Thailand to estimate Holocene ice-volume equivalent sea level change. Quat. Sci. Rev. 137, 54–68.
Briais, A., Patriat, P., Tapponnier, P., 1993. Updated interpretation of magnetic anomalies and seafloor spreading stages in the South China Sea: implications for the Tertiary tectonics of Southeast Asia. J. Geophys. Res. Solid Earth 98, 6299–6328.
Cahill, N., Kemp, A.C., Horton, B.P., Parnell, A.C., 2015. Modeling Sea-level change using errors-in-variables integrated Gaussian processes. Ann. Appl. Stat. 9, 547–571.
Carricart-Ganivet, J.P., 2004. Sea surface temperature and the growth of the West Atlantic reef-building coral *Montastraea annularis*. J. Exp. Mar. Biol. Ecol. 302, 249–260.
Chen, L., Chen, J., Shen, Z., Zhao, J., Li, M.J., Huang, X., Liu, J.B., Zhou, A., 2024. Drought in the Asian summer monsoon region is liked to a weakened inter-hemispheric temperature gradient. Commun. Earth Environ. 5, 432.
Chiba, T., Sugihara, S., Matsushima, Y., Arai, Y., Endo, K., 2016. Reconstruction of Holocene relative sea-level change and residual uplift in the Lake Inba area, Japan. Palaeogeogr. Palaeoclimatol. Palaeoecol. 441, 982–996.
Chua, S., Switzer, A.D., Li, T., Chen, H., Christie, M., Shaw, T.A., Khan, N.S., Bird, M.I., Horton, B.P., 2021. A new Holocene Sea-level record for Singapore. Holocene 31, 1376–1390.
Clark, J.A., Farrell, W.E., Peltier, W.R., 1978. Global changes in postglacial sea level: a numerical calculation. Quat. Res. 9, 265–287.
Contreras-Rosales, L.A., Jennerjahn, T., Steinke, S., Mohtadi, M., Schefuss, E., 2019. Holocene changes in biome size and tropical cyclone activity around the Northern South China Sea. Quat. Sci. Rev. 215, 45–63.
Engelhart, S.E., Horton, B.P., 2012. Holocene sea level database for the Atlantic coast of the United States. Quat. Sci. Rev. 54, 12–25.
Fu, S., Xiong, H., Zong, Y., Huang, G., 2020. Reasons for the low sedimentation and slow progradation in the Pearl River delta, southern China, during the middle Holocene. Mar. Geol. 423, 106133.
Haam, E., Huybers, P., 2010. A test for the presence of covariance between time-uncertain series of data with application to the Dongge Cave speleothem and atmospheric radiocarbon records. Paleoceanography 25, PA2209.
He, C., Ouyang, T., Li, M., Zhu, S., Yu, M., Peng, S., Zhu, Z., Wang, Y., Chen, H., Tian, C., 2024. Nonnegligible contribution of terrigenous sediment inputs from local small watersheds to west regions of the Pearl River Estuary, northern South China Sea shelf. Mar. Geol. 475, 107369.
Hijma, M.P., Engelhart, S.E., Törnqvist, T.E., Horton, B.P., Hu, P., Hill, D.F., 2015. A protocol for a geological sea-level database. In: Shennan, I., Long, A.J., Horton, B. P. (Eds.), Handbook of Sea-Level Research. Wiley-Blackwell, Chichester, pp. 536–553. https://doi.org/10.1002/9781118452547.ch34.
Hijma, M.P., Bradley, S.L., Cohen, K.M., van der Wal, W., Barlow, N.L.M., Blank, B., Frechen, M., Hennekam, R., van Heteren, S., Kiden, P., Mavritsakis, A., Meijninger, B.M.L., Reichart, G.J., Reinhardt, L., Rijsdijk, K.F., Vink, A., Busschers, F. S., 2025. Global sea-level rise in the early Holocene revealed from North Sea peats. Nature 639, 652–657.
Hu, J., Emile-Geay, J., Partin, J., 2017. Correlation-based interpretations of paleoclimate data – where statistics meet past climates. Earth Planet. Sci. Lett. 459, 362–371.
Khan, N.S., Ashe, E., Shaw, T.A., Vacchi, M., Walker, J., Peltier, W.R., Kopp, R.E., Horton, B.P., 2015. Holocene relative sea-level changes from near-, intermediate-, and far-field locations. Curr. Clim. Chang. Rep. 1, 247–262.
Lambeck, K., Rouby, H., Purcell, A., Sun, Y.Y., Sambridge, M., 2014. Sea level and global ice volumes from the Last Glacial Maximum to the Holocene. Proc. Natl. Acad. Sci. USA 111, 15296–15303.
Li, T., Wu, P., 2019. Laterally heterogeneous lithosphere, asthenosphere and sub-lithospheric properties under Laurentia and Fennoscandia from glacial isostatic adjustment. Geophys. J. Int. 216, 1633–1647.
Lin, Y., Kopp, R.E., Xiong, H., Hibbert, F.D., Zheng, Z., Yu, F., Kumar, P., Dangendorf, S., Yi, H., Zhang, Y., 2025. Modern sea-level rise breaks 4,000-year stability in southeastern China. Nature 646, 856–864.
Liu, Z., Lu, Z., Wen, X., Otto-Bliesner, B.L., Timmermann, A., Cobb, K.M., 2014. Evolution and forcing mechanisms of El Niño over the past 21,000 years. Nature 515, 550–553.
Lough, J.M., Barnes, D.J., 2000. Environmental controls on growth of the massive coral *Porites*. J. Exp. Mar. Biol. Ecol. 245, 225–243.
Ma, Y., Qin, Y., Yu, K., Li, Y., Long, Y., Wang, R., Fan, T., Jiang, W., Xu, S., Zhao, J., 2021. Holocene coral reef development in Chenhang Island, Northern South China Sea, and its record of sea level changes. Mar. Geol. 440, 106593.
Mann, T., Bender, M., Lorscheid, T., Stocchi, P., Vacchi, M., Switzer, A.D., Rovere, A., 2019. Holocene sea levels in southeast Asia, Maldives, India and Sri Lanka: the SEAMIS database. Quat. Sci. Rev. 219, 112–125.
Mitrovica, J.X., Milne, G.A., 2002. On the origin of late Holocene sea-level highstands within equatorial ocean basins. Quat. Sci. Rev. 21, 2179–2190.
Parham, P.R., Saito, Y., Sapon, N., Suriadi, R., Mohtar, N.A., 2014. Evidence for ca. 7-ka maximum Holocene transgression on the Peninsular Malaysia east coast. J. Quat. Sci. 29, 414–422.
Pedoja, K., Shen, J.W.S., Kershaw, S., Tang, C., 2008. Coastal Quaternary morphologies on the northern coast of the South China Sea, China, and their implications for current tectonic models: a review and preliminary study. Mar. Geol. 255, 103–117.
Peltier, W.R., Argus, D.F., Drummond, R., 2015. Space geodesy constrains ICE age terminal deglaciation: the global ICE-6G_C (VM5a) model. J. Geophys. Res. Solid Earth 120, 450–487.
Sefton, J.P., Kemp, A.C., Engelhart, S.E., Ellison, J.C., Karegar, M.A., Charley, B., McCoy, M.D., 2022. Implications of anomalous relative sea-level rise for the peopling of Remote Oceania. Proc. Natl. Acad. Sci. USA 119, e2210863119.
Shennan, I., Horton, B., 2002. Holocene land- and sea-level changes in Great Britain. J. Quat. Sci. 17, 511–526.
Shennan, I., Peltier, W.R., Drummond, R., Horton, B., 2002. Global to local scale parameters determining relative sea-level changes and the post-glacial isostatic adjustment of Great Britain. Quat. Sci. Rev. 21, 397–408.
Stanford, J.D., Hemingway, R., Rohling, E.J., Challenor, P.G., Medina-Elizalde, M., Lester, A.J., 2011. Sea-level probability for the last deglaciation: a statistical analysis of far-field records. Glob. Planet. Chang. 79, 193–203.
Stattegger, K., Tjallingii, R., Saito, Y., Michelli, M., Thanh, N.T., Wetzel, A., 2013. Mid to late Holocene sea-level reconstruction of Southeast Vietnam using beachrock and beach-ridge deposits. Glob. Planet. Chang. 110, 214–222.
Stirling, C.H., Andersen, M.B., 2009. Uranium-series dating of fossil coral reefs: Extending the sea-level record beyond the last glacial cycle. Earth Planet. Sci. Lett. 284, 269–283.
Tang, L., Yue, Y., 2023. Application and uncertainty analysis of beachrock to Mid-late Holocene sea-level reconstruction in the northern South China Sea. Mar. Geol. Front. 39 (3), 1–19 (In Chinese with English abstract).
Tang, Y., Chen, G., Peng, Z., Zhang, K., 2011. Late Quaternary tectonics of the Pearl River Delta, SE China: evidence from Xilingang. Geodin. Acta 24, 133–139.
Tjallingii, R., Stattegger, K., Wetzel, A., Phung, V.P., 2010. Infilling and flooding of the Mekong River incised valley during deglacial sea-level rise. Quat. Sci. Rev. 29, 1432–1444.
Tjallingii, R., Stattegger, K., Stocchi, P., Saito, Y., Wetzel, A., 2014. Rapid flooding of the southern Vietnam shelf during the early to mid-Holocene. J. Quat. Sci. 29, 581–588.
Törnqvist, T.E., Bick, S.J., González, J.L., van der Borg, K., de Jong, A.F.M., Kurnik, C.W., 2004. Tracking the sea-level signature of the 8.2 ka cooling event: New constraints from the Mississippi Delta. Geophys. Res. Lett. 31, L23309.
Vacchi, M., Marriner, N., Morhange, C., Spada, G., Fontana, A., Rovere, A., 2016. Multiproxy assessment of Holocene relative sea-level changes in the western Mediterranean: sea-level variability and improvements in the definition of the isostatic signal. Earth Sci. Rev. 155, 172–197.
Vacchi, M., Shaw, T.A., Anthony, E.J., Spada, G., Melini, D., Li, T., Cahill, N., Horton, B. P., 2025. Sea level since the Last Glacial Maximum from the Atlantic coast of Africa. Nat. Commun. 16, 1486.
Wang, Y., Cheng, H., Edwards, R., He, Y., Kong, X., An, Z., Wu, J., Kelly, M., Dykoski, C., Li, X., 2005. The Holocene Asian monsoon: Links to solar changes and North Atlantic climate. Science 308, 854–857.
Wu, M.S., Zong, Y., Mok, K.M., Cheung, K.M., Xiong, H., Huang, G., 2017. Holocene hydrological and sea surface temperature changes in the northern coast of the South China Sea. J. Asian Earth Sci. 135, 268–280.
Xiong, H.X., Zong, Y.Q., Qian, P., Huang, G.Q., Fu, S.Q., 2018. Holocene sea-level history of the northern coast of South China Sea. Quat. Sci. Rev. 194, 12–26.
Xiong, H.X., Zong, Y.Q., Li, T.W., Long, T.W., Huang, G.Q., Fu, S.Q., 2020. Coastal GIA processes revealed by the early to middle Holocene sea level history of East China. Quat. Sci. Rev. 233, 106249.
Yan, T., Yu, K., Jiang, L., Li, Y., Zhao, N., 2024. Significant sea-level fluctuations in the western tropical Pacific during the mid-Holocene. Paleoceanogr. Paleoclimatol. 39, e2023PA004783.
Yan, T., Yu, K., Wang, R., Liu, W., Jiang, L., 2021. Records of sea-level highstand over the Meghalayan age/late Holocene from uranium-series ages of beachrock in Weizhou Island, northern South China Sea. Holocene 31 (11–12), 1745–1760.
Yin, J., Yang, X., Zhou, Q., Li, G., Gao, H., Liu, J., 2021. Sea surface temperature and salinity variations from the end of Last Glacial Maximum (LGM) to the Holocene in the northern South China Sea. Palaeogeogr. Palaeoclimatol. Palaeoecol. 562, 110102.

You, C., Liao, W., Huang, K., Chung, C., Liu, Z., 2024. Sediment source variation using REEs, Sr, and Nd isotopic compositions: a case study in MD05-2901, northwestern South China Sea. Front. Mar. Sci. 10, 1292802.
Yu, K., Chen, T., 2009. Beach sediments from northern South China Sea suggest high and oscillating sea levels during the Late Holocene. Earth Sci. Front. 16, 138–145.
Yu, K., Hua, Q., Zhao, J., Hodge, E., Fink, D., Barbetti, M., 2010. Holocene marine C-14 reservoir age variability: evidence from Th-230-dated corals in the South China Sea. Paleoceanography 25, PA3205.
Yu, K.-F., Zhao, J.-X., Done, T., Chen, T.-G., 2009. Microatoll record for large century-scale sea-level fluctuations in the mid-Holocene. Quat. Res. 71, 354–360.
Yue, Y., Tang, L., 2023. Characteristics of sea Level changes in the northern South China Sea since the Holocene and prediction of the future trends. Mar. Geol. Front. 39 (2), 1–16 (In Chinese with English abstract).
Yue, Y., Tang, L., Yu, K., Huang, R., 2024. Coral records of Mid-Holocene sea-level highstands and climate responses in the northern South China Sea. Acta Oceanol. Sin. 43, 43–57.
Yue, Y., Zhao, Y., Tang, L., Zhang, B., Xiong, H., Zhang, Y., 2025. The sea-level indicative meaning of *Porites* microatolls and its application to middle Holocene sea-level reconstructions in the northern South China Sea. Earth Sci. 50, 3530–3543.
Zhang, Y., Zong, Y., Xiong, H., Li, T., Fu, S., Huang, G., Zheng, Z., 2021. The middle-to-late Holocene relative sea-level history, highstand and levering effect on the east coast of Malay Peninsula. Glob. Planet. Chang. 196, 103369.
Zhang, X., Zheng, Z., Huang, K., Cheng, J., Cheddadi, R., Zhao, Y., Liang, C., Yang, X., Wan, Q., Tang, Y., Chen, C., Li, J., 2023. Quantification of Asian monsoon variability from 68 ka BP through pollen-based climate reconstruction. Sci. Bull. 68, 713–722.
Zong, Y., 2004. Mid-Holocene sea-level highstand along the southeast coast of China. Quat. Int. 117, 55–67.